Nucleation and growth process of atomic layer deposition platinum nanoparticles on strontium titanate nanocuboids

You may also be interested in:

Atomic layer deposition of Pd and Pt nanoparticles for catalysis: on the mechanisms of nanoparticle formation
Adriaan J M Mackus, Matthieu J Weber, Nick F W Thissen et al.

Sub-nanometer dimensions control of core/shell nanoparticles prepared by atomic layer deposition
M J Weber, M A Verheijen, A A Bol et al.

Deposition of uniform Pt nanoparticles with controllable size on TiO2-based nanowires by atomic layer deposition and their photocatalytic properties
Chih-Chieh Wang, Yang-Chih Hsueh, Chung-Yi Su et al.

Deposition of platinum on oxygen plasma treated carbon nanotubes by atomic layer deposition
Yang-Chih Hsueh, Chih-Chieh Wang, Chueh Liu et al.

Influence of surface preparation on atomic layer deposition of Pt films
Ge Liang, Hu Cheng, Zhu Zhiwei et al.

Direct formation of anatase TiO2 nanoparticles on carbon nanotubes by atomic layer deposition and their photocatalytic properties
Sheng-Hsin Huang, Shih-Yun Liao, Chih-Chieh Wang et al.

Control of the initial growth in atomic layer deposition of Pt films by surface pretreatment
Jung Joon Pyeon, Cheol Jin Cho, Seung-Hyub Baek et al.

Applications of atomic layer deposition in solar cells
Wenbin Niu, Xianglin Li, Siva Krishna Karuturi et al.

Nucleation and growth process of atomic layer deposition platinum nanoparticles on strontium titanate nanocuboids

Chuandao Wang[1,2,4]**, Linhua Hu**[2]**, Kenneth Poeppelmeier**[2,3]**,
Peter C Stair**[2,3] **and Laurence Marks**[1]

[1] Department of Materials Science and Engineering, Northwestern University, 2220 North Campus Drive, Evanston, IL 60208-3108, United States of America
[2] Department of Chemistry, Northwestern University, 2145 Sheridan Road, Evanston, IL 60208-3113, United States of America
[3] Chemical Sciences and Engineering Division, Argonne National Laboratory, 9700 South Cass Avenue, Argonne, IL 60439 United States of America

E-mail: ericenkin@gmail.com

Abstract

Uniform, well-dispersed platinum nanoparticles were grown on $SrTiO_3$ nanocuboids via atomic layer deposition (ALD) using (methylcyclopentadienyl)trimethylplatinum ($MeCpPt(Me)_3$) and water. For the first half-cycle of the deposition particles formed through two sequential processes: initial nucleation and growth. The final particle size after a single complete ALD cycle was dependent on the reaction temperature which alters the net Pt deposition per cycle. Additional cycles resulted in further growth of previously formed particles. However, the increase in size per cycle during additional ALD cycles, beyond the first, was significantly lower as less Pt was deposited due to carbonaceous material that partially covers the surface and prevents further $MeCpPt(Me)_3$ adsorption and reaction. The increase in particle size was also temperature dependent due to changes in the net Pt deposition. Pt nanoparticles increased in size by 59% and 76% after 15 ALD cycles for reaction temperatures of 200 °C and 300 °C, respectively. There was minimal change in the number of particles per unit area as a function of reaction time, indicating that there was minimal Ostwald ripening or secondary nucleation for the reaction conditions.

Supplementary material for this article is available online

Keywords: atomic layer deposition, nucleation, growth, TEM

(Some figures may appear in colour only in the online journal)

Introduction

Atomic layer deposition (ALD) is a sequential, self-limiting thin film growth technique which yields angstrom-scale control over film thickness and composition. It relies on self-limiting, sequential binary reactions between gaseous precursor molecules and a substrate, ideally, in a layer by layer fashion [1–3]. However, with materials with high cohesive energies that are less likely to fully wet the substrate, ALD starts by forming well-dispersed uniform nanoparticles, i.e. following Volmer–Weber growth [4, 5]. This has been employed and developed by several research groups for the synthesis of nanostructured metal and metal oxide catalytic materials [6–11]. For instance, Smeds *et al* obtained highly dispersed Ni nanoparticles on Al_2O_3 using several cycles of ALD [10] while Backmen *et al* found that uniform cobalt nanoparticles were deposited on SiO_2 using ALD [11]. It has been shown that ALD can achieve control of the particle size

---

[4] Author to whom any correspondence should be addressed.

[7], composition [12], structure [12, 13], and even exposed surface orientation [13]. However, few studies have focused on developing a detailed description of the nucleation and growth processes during deposition. The influence of reaction temperature and the number of ALD cycles is still not well understood [7, 13–15]. A fundamental understanding of the initial nucleation and subsequent growth versus reaction temperature and the number of ALD cycles will enable control over particle size, dispersion and loading. These properties strongly influence catalyst performance, e.g. Croy *et al* found a strong size dependence for the decomposition of methanol using Pt nanoparticles supported on nanocrystalline anatase TiO_2 [16] while higher performance in methanol reforming was reported by Velu *et al* as a consequence of higher dispersion in Cu-based catalysts [17]; Panagiotopoulou *et al* indicated that the catalytic activity for the water-gas shift reaction increases significantly with metal catalyst loading in a range of 0.1%–5% [18]. Nucleation and growth also influence the quality of ALD-grown thin films as their roughness depends on the number of cycles required for particle coarsening to cover the entire substrate [19].

The specific focus in this work is the first few ALD cycles of Pt deposition onto strontium titanate nanocuboids (STO-NCs), which is in powder form used as substrates [20]. The synthesis of Pt on the STO-NCs (Pt/STO-NCs) is of particular interest as this system can serve as a model catalyst, e.g. recently the ALD Pt/STO system was found to have exceptional activity and stability as a combustion catalyst [21]. In addition, STO acts as a UV photocatalyst similar to TiO_2 [22], in which photons generate electron–hole pairs that catalyze reactions to produce fuels such as hydrogen or methanol. The success of the Pt/STO system in these applications depends upon the STO support. The STO-NCs used here were synthesized by a sol precipitation-hydrothermal treatment procedure with oleic acid as the surfactant. The resulting cuboid shape is believed to be a consequence of the elastic constraints in the lamellar liquid structure established during the hydrothermal process [20]. The as-prepared STO-NCs are useful as a catalyst support for fundamental studies as a consequence of being nonporous, single crystalline with (100) facet mainly exposed, with a pure SrO termination [23]. The narrow, nanoscale size distribution, ∼20 nm, yields a medium-high BET surface area of $70\,m^2\,g^{-1}$ [20], compared to macroscopic single-crystal substrates with lower surface area [24] or high-surface-area supports with amorphous shape or an undetermined exposed surface termination [25].

Experimental section

ALD was carried out in a continuously pumped, viscous flow reaction chamber with a base pressure of 0.3 Torr and an operating pressure of 1.0 Torr. The chamber is equipped for gas phase dosing with several precursors including $MeCpPtMe_3$ (Sigma-Aldrich 99%), which delivers Pt to the surface, and water that regenerates surface hydroxyl groups after the Pt precursor exposure. The precursors were stored in bubblers held at temperatures to achieve sufficient vapor

pressure and reasonable dosing times ($MeCpPtMe_3$ 50 °C ∼0.8 Torr and H_2O at room temperature ∼25 Torr). Nitrogen (N_2), with a flow rate of 5 and 40 standard cubic centimeters per min (sccm), was used to transport the $MeCpPtMe_3$ and water to the reaction chamber. Before deposition, all STO substrates were pretreated with ozone for 15 min at 200 °C in order to completely remove oleic acid ligands remaining from the STO synthesis, as confirmed by *ex situ* x-ray photoelectron spectroscopy (XPS) and transmission electron microscopy (TEM). The timing sequence for Pt ALD is expressed as t_1–t_2–t_3–t_4, where t_1 was the Pt precursor dosing time, t_2 the time used for purging the reactor with N_2, t_3 the water dosing time and t_4 the second N_2 purge time. The timing sequence used for these studies was 300 s–600 s–120 s–600 s. For one cycle, a total exposure of approximately 9×10^4 L ($1\,L = 10^{-6}$ Torr sec) of the Pt precursor was dosed into the reaction chamber.

The size and morphology of the as-synthesized Pt nanoparticles were determined by conventional high-resolution and high-angle annular dark field electron microscopy (HREM, HAADF) using a JOEL2100 at 200 kV. The TEM samples were prepared using several drops of ethanol-dispersed Pt/STO applied to the surface of a carbon film supported on a copper grid [26, 27]. The Pt weight loading, overall Pt/STO composition and chemical state were analyzed using inductively coupled plasma-atomic emission spectroscopy (ICP-AES) and XPS.

Results and discussion

Structural characterization revealed that ALD was an efficient method to deposit highly dispersed Pt nanoparticles on the STO surfaces. Figure 1 is a typical HAADF image with an inner collection angle (124 mRad) of Pt/STO-NCs after a single cycle ALD at 300 °C and shows discrete Pt nanoparticles on the STO surface. We note that with this inner collection angle the contrast will scale as the projected atomic number to some power, sometimes called 'Z-contrast'. The Pt particle size through ALD deposition was typically around 1–3 nm, so the role of the electron probe size (∼0.2–1.5 nm) in altering the apparent size needs to be taken into account, it is inadvisable to simply assume that the apparent size is correct.

A complete description of the probe in a STEM is complex, and involves both electron optical contributions such as the mutual coherence of the source, the diameter and demagnification of the field-emission tip as well as the alignment, defocus, objective aperture size, vibration and drift. As a rough guide one can consider the effect of various resolution limiting terms via a conventional statistically random sum of terms, i.e. the square root of the sum of the squares, but this is not rigorously correct. While the true probe may have been calibrated when the instrument was first installed, for instance by using a sharp edge, it varies with time and is only approximately known. For a larger probe size, primarily determined by the objective aperture size and demagnification, terms such as vibration are small, and many
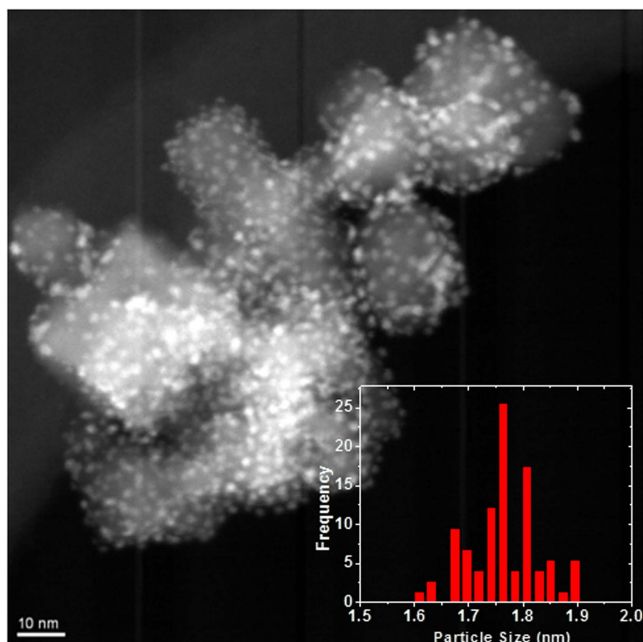
Figure 1. A typical HAADF image of Pt/STO-NCs obtained with 1 cycle at 300 °C. A size distribution histogram is inserted. In the image, the light gray and cuboid shapes are the STO-NCs, the bright area on STO-NCs are the Pt nanoparticles. Note that the cuboid nature of the STO is only apparent when they are tilted to {001}, not random orientations as in the figure.

instruments provide a user-variable multi-position switch, which varies the size linearly following a parameter *p*. This parameter is proportional to the true probe size but not a rigorously accurate measurement of it. For fully incoherent imaging, which requires a large inner and outer collection angle as used here, the image of a nanoparticle will be the convolution of the probe and the intensity across the particle.

A series of HAADF images (supplemental materials is available online at stacks.iop.org/NANO/28/185704/mmedia) of Pt/STO (1 cycle, 300 °C) were taken with different instrument reported probe sizes, and the results are summarized in figure 2(a). The measured sizes based on the full width of the line intensity profile across ∼80 Pt NPs from two different sample areas. For each measurement, the HAADF image only selected areas with individually dispersed Pt particles; for non-spherical NPs, the reported size is the average of the largest and smallest measured diameters. From figure 2(a), it can be seen that the measured particle size depends linearly on the parameter *p*. Figure 2(b) suggests that measured particle size/probe size relationship is solely microscope dependent, as would be expected. A linear fit to all of the plotted data in figure 2(b) produced the following relationship between *p* and the measured particle size:

$$M(p) = 0.46p + R, \qquad (1)$$

where $M(p)$ is the measured particle size, *p* is the probe size and *R* is the real size. From the equation above, the real particle size can be determined from a knowledge of the instrument settings by extrapolating to a nominal zero probe size. We note that unless this extrapolation is done HAADF images may yield inaccurate measurements of the size.

The nucleation and growth mechanisms of ALD-deposited Pt/STO-NCs were investigated by recording a series of HAADF images. In the following, we will first discuss the nucleation process, starting with the initial surface reaction. As shown by Setthapun *et al* to initiate Pt ALD on an oxide substrate two requirements need to be satisfied: (1) adsorption of the Pt precursor MeCpPtMe$_3$, and (2) elimination of the precursor ligands [28]. Initially, MeCpPtMe$_3$ can absorb onto a carbon-free surface by exchange between surface hydroxyl groups and the methyl ligands on the precursor [29]. The limiting step in the deposition is the elimination of the remaining precursor ligands which is difficult compared to adsorption, and is usually performed by thermal decomposition or oxidation following the purge with flowing N$_2$. Once the ligands are eliminated, the adsorbed precursor is reduced to zero valent metal atoms [28]. Since single atoms are not energetically stable on the surface and will diffuse to form clusters, subsequent surface diffusion leads to the nucleation of Pt nanoparticles on the oxide surface. To determine how the Pt particle size depends on the amount deposited in the initial half-cycle, a series of samples were prepared using various dosing times at 200 °C. The particle size and density as a function of Pt precursor dosing time are shown in figure 3 for samples removed immediately from the reaction chamber after N$_2$ purging. The measured particle density is based on the number of particles per unit area counted in the HAADF images with the assumption that Pt particles were uniformly deposited on the top and bottom STO-NCs surfaces. Particles with an average diameter of 0.69 nm were formed by a 0.5 s dose, and the particle density increased by only 30% between 0.5 and 2 s then saturated at doses of ∼10 s. This suggests that the nucleation process required less than 0.5 s, and the entire nucleation process was completed after a 10 s Pt precursor dose. The critical nucleation diameter (D_c) has to be less than or equal to the smallest observed diameter of 0.69 nm. According to classical nucleation theory, the critical radius for Pt nucleation on a metal oxide surface depends on the interfacial energy and surface temperature (appendix 2) as,

$$D_C = \frac{4\gamma_{pg}}{|\Delta G_V|}, \qquad (2)$$

where γ is the interfacial energy and the subscripts 'pg' refer to Pt-gas and ΔG_V is free energy of formation per unit volume of Pt clusters formed from isolated Pt atoms. An estimate of the critical nucleation diameter for Pt is 0.4–0.6 nm (2–8 atoms) (supplemental material) which is consistent with the measured particle size produced by a 0.5 s dose. As the nucleation process will consume Pt atoms around the newly formed cluster, the Pt concentration will fall below the minimum required for nucleation, i.e. a depletion zone will be formed. With additional Pt deposition nucleation stops whereas growth continues. As shown in figure 3, the Pt nanoparticle size increased with MeCpPtMe$_3$ exposure, reaching 1.39 nm after dosing for 2 s. The migration distance of a single surface Pt atom over the time of a single ALD cycle (>300 s) is 5–740 nm for a reaction temperature of 125 °C–300 °C (see supplemental material). This is much larger than the distance between nuclei (∼5–10 nm). Thus, all
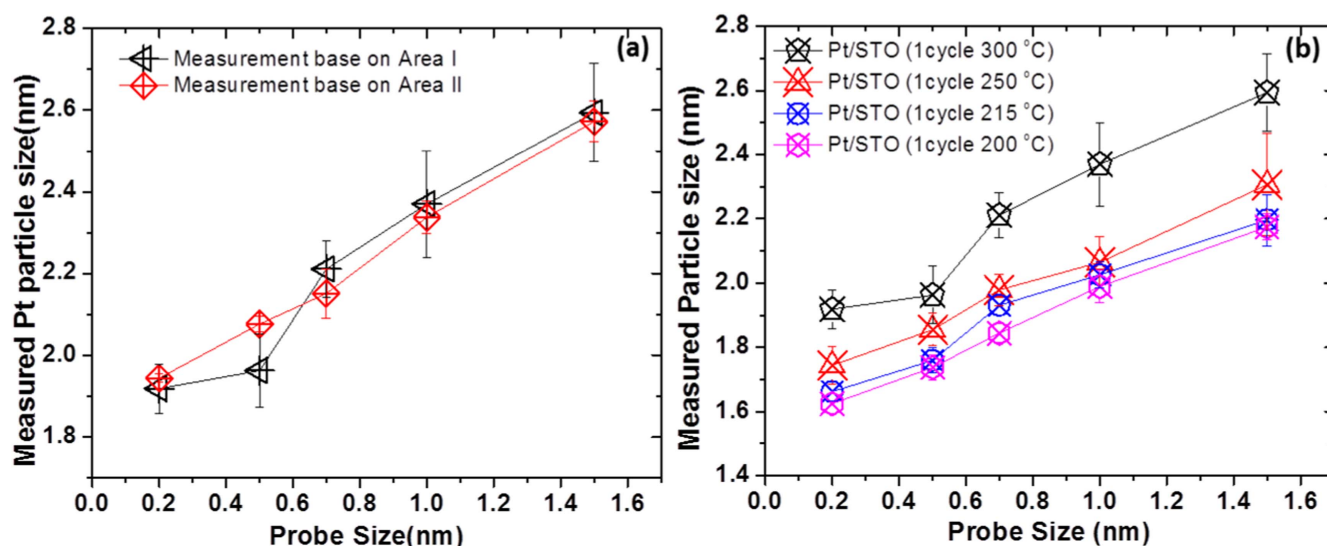
Figure 2. Measured nanoparticle size as a function of the microscope probe size with measurement based on (a) different sample area of Pt/STO (1 cycle 300 °C) (b) series of Pt/STO syntheses with 1 cycle at different reaction temperatures. The error bar shown here is the standard deviation of each measurement.
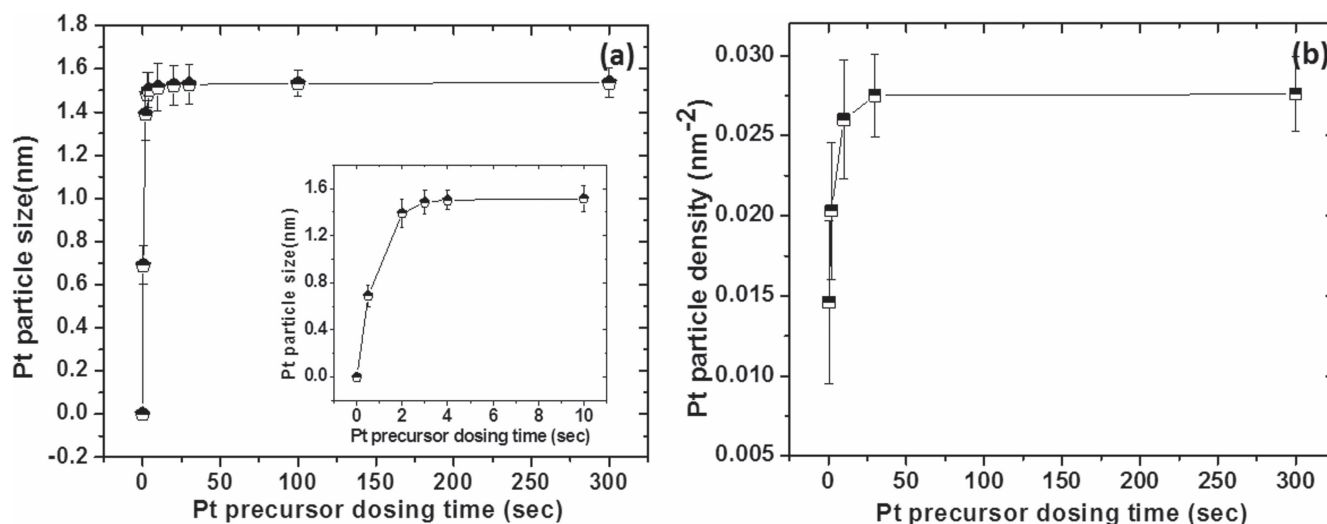
Figure 3. (a) Pt particle size and (b) particle density dependence on Pt precursor dosing time measured from HAADF images. The insert shows an expanded view of the data near the origin. The error bar depicts the statistical standard deviation of each measurement.

of the Pt atoms can easily diffuse from the initial adsorption sites to existing Pt nuclei.

The growth of the Pt nanoparticles after the first complete ALD cycle was mainly dependent on the amount of Pt deposited and to a lesser extent on the particle density, both of which depend on the reaction temperature. The size change depends on the net Pt deposition is supported by the following analyses. First, as shown in figure 3, the particle size changed with dosing time, hence the amount of deposited Pt, until the adsorption was saturated (~5 s). Second, the Pt mass computed by counting particles was compared with the mass measured by ICP-AES. ICP-AES measurements showed that the Pt weight loading after the first cycle increased with reaction temperature over the range 125 °C–300 °C from 1.94% to 7.53%, figure 4(c). The Pt mass obtained by counting nanoparticles and scaled to 1 g STO-NCs is also

included in figure 4(a). The mass was calculated as,

$$\text{wt}\% = \frac{2}{3}\pi R^3 \rho_N S, \tag{3}$$

where R is the particle radius, ρ_N is the particle density per unit area measured from HAADF images (figures 4(a), (b)) and S is the BET surface area per unit mass of STO-NCs (~70 m^2 g^{-1}). This result indicates that essentially all the deposited Pt was present in the observable nanoparticles. According to equation (3), the particle size was determined by deposited Pt loading and particle density. As shown in figure 4(b), increasing the reaction temperature from 125 °C to 300 °C the particle density only increased slightly (~13%), which is much smaller than the variation of Pt loading (~288%). Thus the increase of particle size was predominantly determined by the amount of Pt deposited, which was dependent on reaction temperature. We hypothesize that
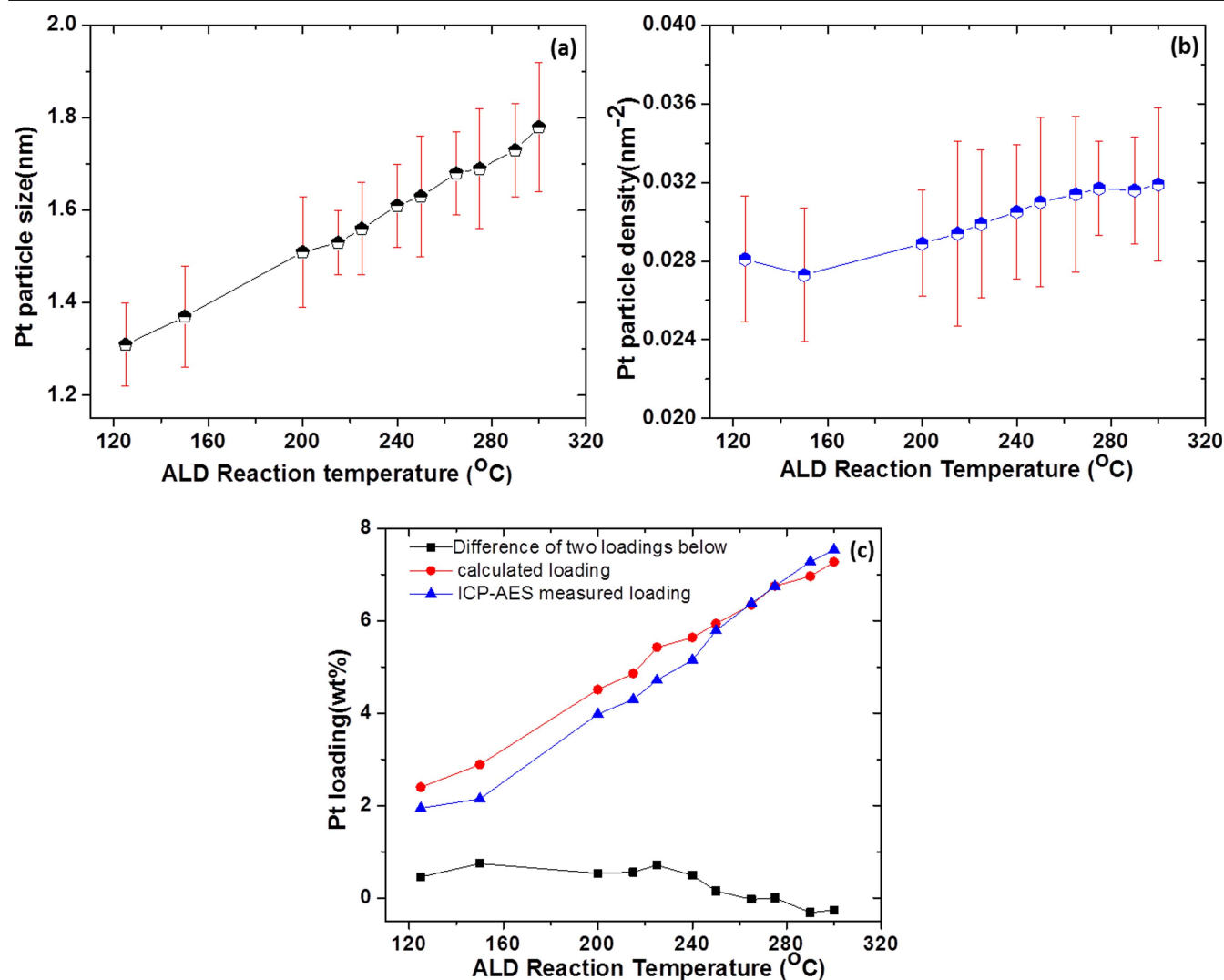
Figure 4. Platinum (a) particle size and (b) particle density as a function of the ALD reaction temperature after single cycle synthesis. (c) Pt weight loading as a function of ALD reaction temperature. The black curve shows the difference between the values obtained by counting particles and by ICP-AES. The error bars in (a) and (b) are statistical standard deviations.

as reaction temperature increased, more precursor ligand fragments are eliminated and more unoccupied surface is available for MeCpPtMe$_3$ molecules to adsorb [28].

After considering the growth during the 1st cycle, we turn to the case of a series of cycles. The influence of multiple ALD cycles on particle size is shown in figure 5. The graph illustrates that the particle size at both 200 °C and 300 °C increased with the number of ALD cycles. However, the Pt particle growth in the subsequent cycles was significantly lower than for the first cycle. This difference is likely due to a carbonaceous layer that partially covers the STO surface after the first cycle. The major contribution to this layer is ligands from previous cycles that have not been completely removed [15, 28]. While oxygen is the second reagent commonly used in Pt ALD [13, 15], water was used here to generate hydroxyl groups on the oxide surface to react with the Pt precursor [28, 30, 31]. However, the removal of carbonaceous layers using water as the second reagent in ALD is not expected to be as efficient as using oxygen or ozone. Figure 6(a) shows the C1s/Ti2p ratio from XPS
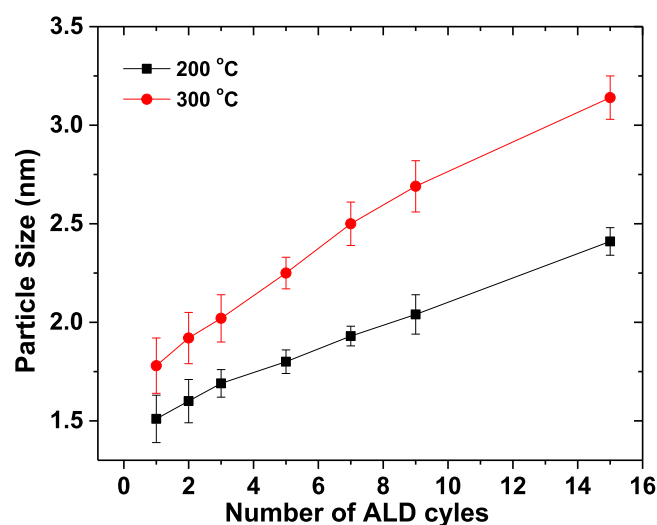
Figure 5. Pt particle size as a function of the number of ALD cycles measured from HAADF images.
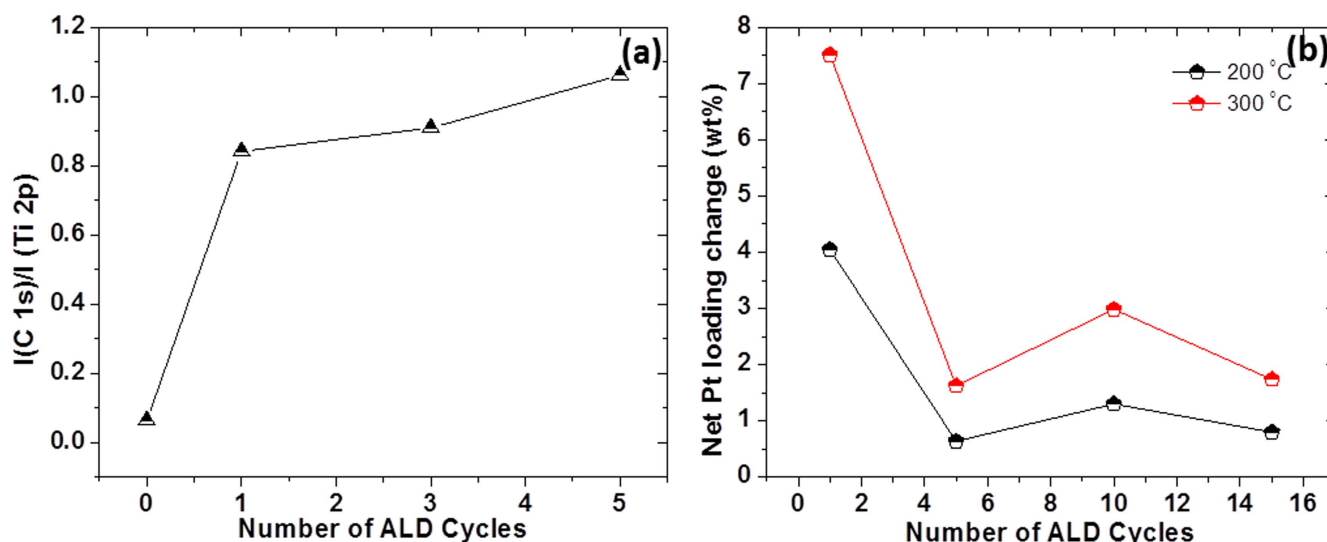
Figure 6. (a) C1s/Ti2p ratios from XPS measurements of Pt/STO-NCs deposited with different numbers of ALD cycles. (b) ICP-AES measured net Pt loading change during a specific number of cycle.
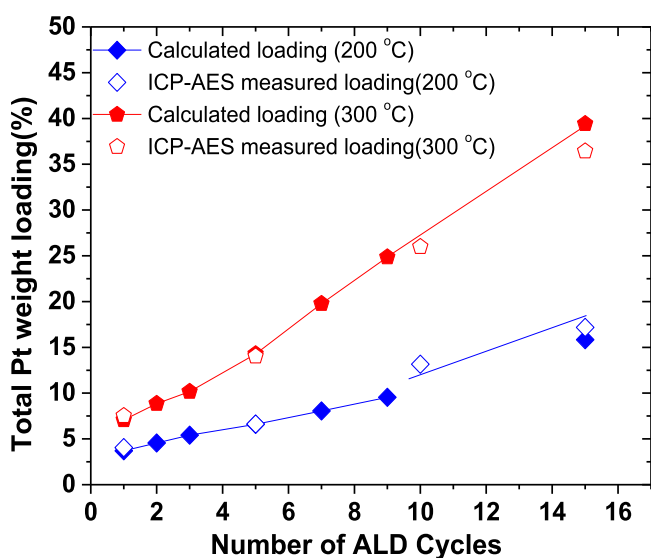
Figure 7. Comparison of Pt loadings measured by ICP-AES and by counting particles in HAADF images as a function of the number of Pt/STO ALD cycles prepared at 200 °C and 300 °C.

measurements of as-synthesized STO samples before and after 1, 3, and 5 cycles of Pt ALD at 200 °C. An obvious increase of carbon was observed after the first Pt ALD cycle. The C1s/Ti2p ratio after 3 and 5 cycles of Pt ALD was essentially the same as after the first cycle, which implies that the residual carbonaceous layer reached a steady-state coverage (~0.78 ML if in a graphene structure) that was dependent on the reaction temperature and purge conditions after the initial Pt ALD cycle. As a result, the Pt deposited during subsequent cycles was much lower than that deposited by the 1st cycle as verified by the ICP measurements shown in figure 6(b). For multiple ALD cycles (1–15), the particle density did not change significantly (<3%, supplemental material) which suggests that secondary nucleation or particle coalescence was minimal. Using equation (3), the total Pt masses determined by ICP-AES and observed as particles are

plotted together in figure 7. From this plot it is clear that all of the deposited Pt appears in the particles and particle size increase in a certain cycle is solely determined by the amount Pt deposited.

A schematic representation of Pt nanoparticle formation from the 1st cycle and the *N*th (*N* > 1) cycle is shown in figure 8, based on our results. The particles are formed through two processes: nucleation and growth, and the increase in particle size from each cycle is determined solely by the additional Pt deposited during that cycle. Although this growth mechanism is based upon our data for the Pt/STO-NCs system, the analysis can almost certainly be generalized to other ALD syntheses.

Conclusions

In summary, ALD synthesized platinum nanoparticles supported on $SrTiO_3$ nanocuboid surfaces are ultrafine and well-dispersed. From HAADF imaging, it has been shown that the electron probe size influences the apparent particle size measurements but this can be taken into account by appropriate calibration measurements. During the initial cycle of ALD the deposition process begins with nucleation followed by growth, both occurring on a time scale that is fast relative to the deposition time. The temperature dependence of the final size is a consequence predominantly of the amount of Pt deposited. With multiple cycles, the particle size increases with the number of ALD cycles and the increase in size per cycle is also determined by the incremental amount of Pt deposited. The incremental increase in size per cycle is significantly lower than that for the first cycle. This is likely due to carbonaceous material left on the surface from decomposition of the $MeCpPt(Me)_3$ ligands. This growth model should not be limited to Pt nanoparticles on STO-NCs surfaces but is expected to apply to other systems.
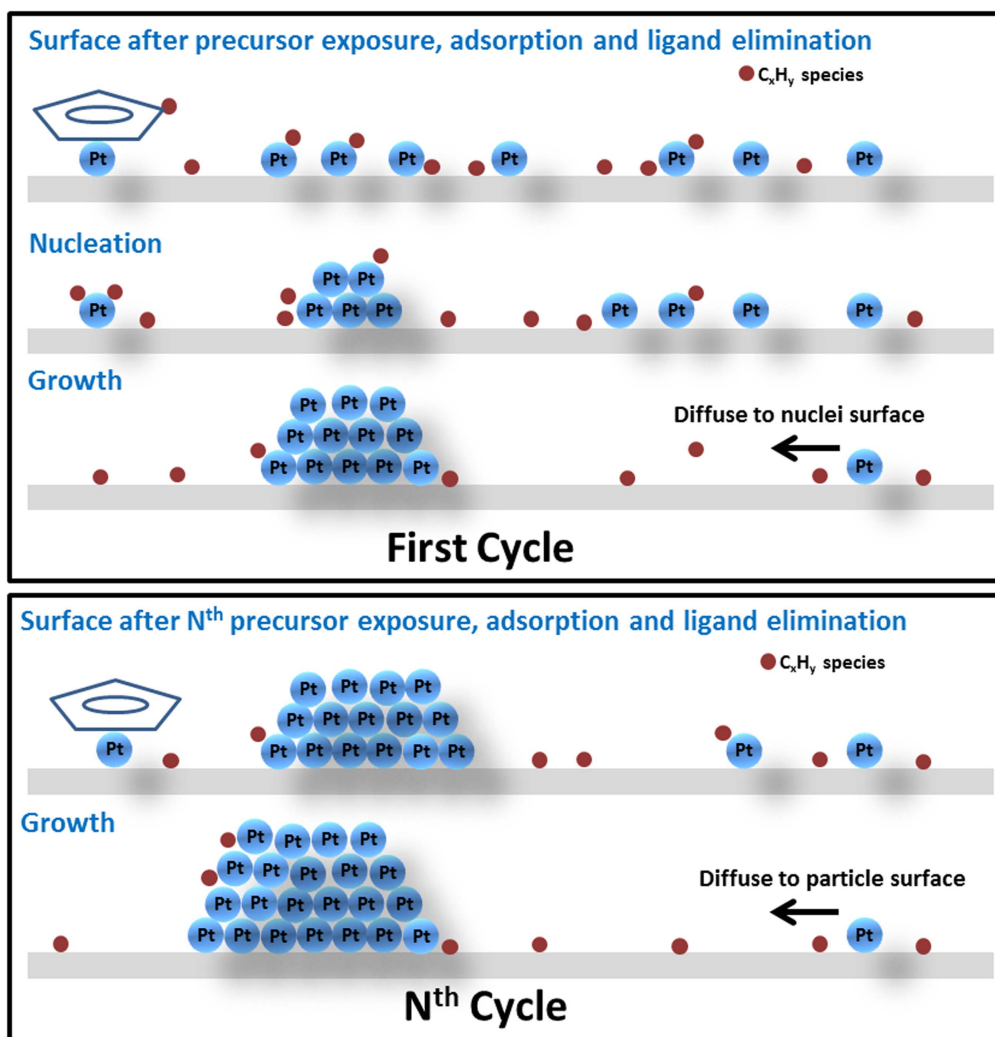
Figure 8. Schematic representation of Pt particle formation and growth on oxide surface for 1st and multiple ALD cycles.

Acknowledgments

References

[1] Puurunen R L 2005 Surface chemistry of atomic layer deposition: a case study for the trimethylaluminum/water process *J. Appl. Phys.* **97** 121301

[2] Hirvikorpi T, Vaha-Nissi M, Mustonen T, Iiskola E and Karppinen M 2010 Atomic layer deposited aluminum oxide barrier coatings for packaging materials *Thin Solid Films* **518** 2654–8

[3] Proslier T, Klug J A, Elam J W, Claus H, Becker N G and Pellin M J 2011 Atomic layer deposition and superconducting properties of nbsi films *J. Phys. Chem.* C **115** 9477–85

[4] Shrestha P, Gu D, Tran N H, Tapily K, Baumgart H and Namkoong G 2010 Investigation of Volmer–Weber growth during the nucleation phase of ald platinum thin films and template based platinum nanotubes *ECS Trans.* **33** 127–34

[5] Hinch B J and Dubois L H 1991 Water-adsorption on Cu(111) —evidence for Volmer–Weber film growth *Chem. Phys. Lett.* **181** 10–5

[6] Herrera J E, Kwak J H, Hu J Z, Wang Y, Peden C H F, Macht J and Iglesia E 2006 Synthesis, characterization, and catalytic function of novel highly dispersed tungsten oxide catalysts on mesoporous silica *J. Catalysis* **239** 200–11

[7] Christensen S T *et al* 2009 Controlled growth of platinum nanoparticles on strontium titanate nanocubes by atomic layer deposition *Small* **5** 750–7

[8] King J S, Wittstock A, Biener J, Kucheyev S O, Wang Y M, Baumann T F, Giri S K, Hamza A V, Baeumer M and Bent S F 2008 Ultralow loading Pt nanocatalysts prepared by atomic layer deposition on carbon aerogels *Nano Lett.* **8** 2405–9

[9] Keranen J, Auroux A, Ek S and Niinisto L 2002 Preparation, characterization and activity testing of vanadia catalysts deposited onto silica and alumina supports by atomic layer deposition *Appl. Catalysis* A **228** 213–25

[10] Smeds S, Salmi T, Lindfors L P and Krause O 1996 Chemisorption and Tpd studies of hydrogen on Ni/Al$_2$O$_3$ *Appl. Catalysis* A **144** 177–94

[11] Backman L B, Rautiainen A, Lindblad M, Jylha O and Krause A O I 2001 Characterisation of Co/SiO$_2$ catalysts prepared from Co(Acac)(3) by gas phase deposition *Appl. Catalysis* A **208** 223–34

[12] Lei Y *et al* 2012 Synthesis of Pt–Pd core–shell nanostructures by atomic layer deposition: application in propane oxidative dehydrogenation to propylene *Chem. Mater.* **24** 3525–33

[13] Enterkin J A, Poeppelmeier K R and Marks L D 2011 Oriented catalytic platinum nanoparticles on high surface area strontium titanate nanocuboids *Nano Lett.* **11** 993–7

[14] Mackus A J M, Verheijen M A, Leick N, Bol A A and Kessels W M M 2013 Influence of oxygen exposure on the nucleation of platinum atomic layer deposition: consequences for film growth, nanopatterning, and nanoparticle synthesis *Chem. Mater.* **25** 1905–11

[15] Mackus A J M, Leick N, Baker L and Kessels W M M 2012 Catalytic combustion and dehydrogenation reactions during atomic layer deposition of platinum *Chem. Mater.* **24** 1752–61

[16] Croy J R, Mostafa S, Liu J, Sohn Y H and Cuenya B R 2007 Size dependent study of MeOH decomposition over size-selected Pt nanoparticles synthesized via micelle encapsulation *Catalysis Lett.* **118** 1–7

[17] Velu S, Suzuki K, Okazaki M, Kapoor M P, Osaki T and Ohashi F 2000 Oxidative steam reforming of methanol over Cuznal(Zr)-oxide catalysts for the selective production of hydrogen for fuel cells: catalyst characterization and performance evaluation *J. Catalysis* **194** 373–84

[18] Panagiotopoulou P and Kondarides D I 2004 Effect of morphological characteristics of TiO$_2$-supported noble metal catalysts on their activity for the water-gas shift reaction *J. Catalysis* **225** 327–36

[19] Mack J F, Van Stockum P B, Yemane Y T, Logar M, Iwadate H and Prinz F B 2012 Observing the nucleation phase of atomic layer deposition *in situ Chem. Mater.* **24** 4357–4362

[20] Hu L H, Wang C D, Lee S, Winans R E, Marks L D and Poeppelmeier K R 2013 SrTiO$_3$ nanocuboids from a lamellar microemulsion *Chem. Mater.* **25** 378–84

[21] Enterkin J A, Setthapun W, Elam J W, Christensen S T, Rabuffetti F A, Marks L D, Stair P C, Poeppelmeier K R and Marshall C L 2011 Propane oxidation over Pt/SrTiO$_3$ nanocuboids *ACS Catalysis* **1** 629–35

[22] Linsebigler A L, Lu G Q and Yates J T 1995 Photocatalysis on TiO$_2$ surfaces—principles, mechanisms, and selected results *Chem. Rev.* **95** 735–58

[23] Lin Y Y, Wen J G, Hu L H, Kennedy R M, Stair P C, Poeppelmeier K R and Marks L D 2013 Synthesis-dependent atomic surface structures of oxide nanoparticles *Phys. Rev. Lett.* **111** 156101

[24] Christensen S T, Elam J W, Lee B, Feng Z, Bedzyk M J and Hersam M C 2009 Nanoscale structure and morphology of atomic layer deposition platinum on SrTiO$_3$ (001) *Chem. Mater.* **21** 516–21

[25] Lu J L and Stair P C 2010 Nano/subnanometer Pd nanoparticles on oxide supports synthesized by AB-type and low-temperature ABC-type atomic layer deposition: growth and morphology *Langmuir* **26** 16486–95

[26] Lee Y W, Ko A R, Han S B, Kim H S and Park K W 2011 Synthesis of octahedral Pt–Pd alloy nanoparticles for improved catalytic activity and stability in methanol electrooxidation *Phys. Chem. Chem. Phys.* **13** 5569–72

[27] Yung T Y, Lee J Y and Liu L K 2013 Nanocomposite for methanol oxidation: synthesis and characterization of cubic Pt nanoparticles on graphene sheets *Sci. Technol. Adv. Mater.* **14** 035001

[28] Setthapun W *et al* 2010 Genesis and evolution of surface species during Pt atomic layer deposition on oxide supports characterized by *in situ* XAFS analysis and water-gas shift reaction *J. Phys. Chem.* C **114** 9758–71

[29] Christensen S T E and J W 2010 Atomic layer deposition of Ir–Pt alloy films *Chem. Mater.* **22** 2517–25

[30] Yermakov Y I 1976 Supported catalysts obtained by interaction of organometallic compounds of transition-elements with oxide supports *Catalysis Rev.* **13** 77–120

[31] Kessels W M M, Knoops H C M, Dielissen S A F, Mackus A J M and van de Sanden M C M 2009 Surface reactions during atomic layer deposition of Pt derived from gas phase infrared spectroscopy *Appl. Phys. Lett.* **95** 013114